Accepted for publication in the ApJ
Preprint typeset using LaTeX style emulateapj v. 5/2/11

arXiv:1407.3505v1 [astro-ph.GA] 13 Jul 2014

# EFFECTS OF SPIRAL ARMS ON STAR FORMATION IN NUCLEAR RINGS OF BARRED-SPIRAL GALAXIES

Woo-Young Seo and Woong-Tae Kim
Center for the Exploration of the Origin of the Universe (CEOU), Astronomy Program, Department of Physics & Astronomy, Seoul National University, Seoul 151-742, Republic of Korea

*Accepted for publication in the ApJ*

## ABSTRACT

We use hydrodynamic simulations to study the effect of spiral arms on the star formation rate (SFR) occurring in nuclear rings of barred-spiral galaxies. We find that spiral arms can be an efficient means of gas transport from the outskirts to the central parts, provided that the arms are rotating slower than the bar. While the ring star formation in models with no-arm or corotating arms is active only during about the bar growth phase, arm-driven gas accretion makes the ring star formation both enhanced and prolonged significantly in models with slow-rotating arms. The arm-enhanced SFR is larger by a factor of $\sim 3-20$ than in the no-arm model, with larger values corresponding to stronger and slower arms. Arm-induced mass inflows also make dust lanes stronger. Nuclear rings in slow-arm models are $\sim 45\%$ larger than in the no-arm counterparts. Star clusters that form in a nuclear ring exhibit an age gradient in the azimuthal direction only when the SFR is small, whereas no noticeable age gradient is found in the radial direction for models with arm-induced star formation.

*Subject headings:* galaxies: ISM — galaxies: kinematics and dynamics — galaxies: nuclei — galaxies: spiral — ISM: general — stars: formation

## 1. INTRODUCTION

Barred-spiral galaxies often host star-forming nuclear rings at their centers (e.g., Phillips 1996; Buta & Combes 1996; Knapen et al. 2006; Mazzuca et al. 2008; Comerón et al. 2009; Sandstrom et al. 2010; Mazzuca et al. 2011; Hsieh et al. 2011; van der Laan et al. 2011). These rings are most likely produced by the radial infall of gas at large radii caused by angular momentum loss due to its nonlinear interactions with an underlying stellar bar potential (e.g, Combes & Gerin 1985; Shlosman et al. 1990; Athanassoula 1992; Heller & Shlosman 1994; Knapen et al. 1995; Buta & Combes 1996; Kim et al. 2012b; Kim & Stone 2012). They appear smaller in more strongly barred galaxies (e.g., Comerón et al. 2010) and unrelated to resonances with the bars (e.g., Piñol-Ferrer et al. 2014). This suggests that the ring location is determined primarily by the amount of angular momentum loss rather than the resonances, as confirmed by numerical simulations (e.g., Kim et al. 2012a,b). Large gas surface density and small dynamical timescale of nuclear rings make them one of the most intense star forming regions in disk galaxies.

Observations indicate that the star formation rate (SFR) in a nuclear ring varies widely from galaxy to galaxy (e.g., Mazzuca et al. 2008; Comerón et al. 2010), although the total gas content in a ring is similar at $\sim (1-6)\times 10^8$ $M_\odot$ (e.g., Buta et al. 2000; Benedict et al. 2002; Sheth et al. 2005; Schinnerer et al. 2006). Data presented in Mazzuca et al. (2008) and Comerón et al. (2010) suggest that strongly barred galaxies tend to have a small SFR, while weakly barred galaxies have a wide range of SFR at $\sim 0.1-10$ $M_\odot$ yr$^{-1}$. Ring star formation appears to be long lived, occurring either continuously (van der Laan et al. 2013) or episodically (Allard et al. 2006; Sarzi et al. 2007) for $\sim 1-3$ Gyr. In some galaxies, young star clusters exhibit an azimuthal age gradient such that they tend to be older farther away from the contact points between a ring and dust lanes, while there is no noticeable age gradient in many other galaxies (e.g, Böker et al. 2008; Mazzuca et al. 2008; Ryder et al. 2010; Brandl et al. 2012). Yet, what determines the ring SFR as well as the presence or absence of the azimuthal age gradient along a ring is not clearly understood.

In a recent attempt to understand these observational results, Seo & Kim (2013, hereafter Paper I) ran hydrodynamic simulations for star formation occurring in nuclear rings of barred galaxies without spiral arms, and found that the ring SFR is controlled mainly by the mass inflow rate to the ring rather than the total gas mass in the ring. In these bar-only models, the massive gas inflows caused by the bar growth result in a strong burst phase of SFR that lasts only for $\sim 0.2$ Gyr, after which both the mass inflow rate and SFR are decreased to very small values below $\sim$ 0.1 $M_\odot$ yr$^{-1}$. The main reason for this short burst of star formation is that only the gas inside the bar region (more precisely, inside the outermost $x_1$ orbit) can respond to the bar potential to initiate the rapid gas infall, while the gas outside the bar is not much affected by the bar potential (e.g, Kim et al. 2012b; Kim & Stone 2012). Paper I also found that an azimuthal age gradient of young star clusters is expected when the SFR is less than a critical value affordable at the contact points. These bar-only models may explain ring star formation in galaxies with low SFR, but would require that the bars should be dynamically young in galaxies with high SFR, which is quite unlikely since the lifetime of bars is quite long (several Gyrs) in observations (e.g., Gadotti & de Souza 2005; Pérez et al. 2009) and $N$-body simulations (e.g., Shen & Sellwood 2004; Bournaud et al. 2005; Berentzen et al. 2007; Athanassoula et al. 2013).

If the mass inflow rate to the ring is really a critical factor in determining the ring SFR, long-lived star

seowy@astro.snu.ac.kr, wkim@astro.snu.ac.kr

formation requires that fresh gas should be supplied to the nuclear rings continually or continuously. There are several additional gas-feeding mechanisms at work in real galaxies that may change the temporal evolution of the SFR considerably. These include galactic fountains (e.g, Fraternali & Binney 2006, 2008), cosmic accretion of primordial gas (e.g, Dekel et al. 2009; Richter 2012), and angular momentum dissipation by spiral arms (e.g., Roberts & Shu 1972; Lubow et al. 1986; Hopkins et al. 2011; Kim & Kim 2014). For instance, Fraternali & Binney (2008) estimated the gas infalling rates of $\sim 2.9$ and $\sim 0.8$ $M_\odot$ yr$^{-1}$ for NGC 891 and NGC 2403, respectively, most of which was ejected to the halos via supernova (SN) feedback, while Richter (2012) found high velocity clouds feed a normal galactic disk with gas at a rate of $\sim 0.7$ $M_\odot$ yr$^{-1}$. Since the gas supply in the form of fountains and cosmic accretion occurs over a whole disk plane, the accreted gas should make its way to the galaxy center anyway to help promote star formation in the rings. Very recently, Kim & Kim (2014) showed that stellar spiral arms can play such a role, transporting the gas inward at a rate $\sim 0.05 - 3.0$ $M_\odot$ yr$^{-1}$ depending on the arm strength and pattern speed, which can potentially enhance the ring SFR.

In this paper, we investigate star formation in a nuclear ring of a disk galaxy that possesses both spiral arms and a bar. This is a straightforward extension of Paper I that considered only the bar potential. By varying the arm strength and pattern speed while fixing the bar parameters, we quantity the effect of the spiral arms on the ring SFR and gaseous structures that form. In Section 2, we describe our galaxy models and numerical method. In Section 3, we present the results on overall evolution of our galaxy models, star formation occurring in nuclear rings, and age gradients of star clusters. We summarize and discuss our results in Section 4.

## 2. MODEL AND METHOD

We consider disk galaxies with both spiral arms and a bar. Our galaxy models are identical to those in Paper I except that we initially consider an exponential gaseous disk rather than a uniform disk and that we additionally include stellar spiral perturbations. The reader is referred to Paper I for the detailed description of the simulation setups and numerical methods. Here we briefly describe our current models and methods.

The gaseous disk is infinitesimally-thin, self-gravitating, unmagnetized, and rotating about the galaxy center. The initial profile of gas surface density is taken to

$$\Sigma_0 = 29.4 \exp(-R/9.7\,\mathrm{kpc})\ M_\odot\ \mathrm{pc}^{-2}, \quad (1)$$

which describes nearby disk galaxies reasonably well (Bigiel & Blitz 2012). We adopt an isothermal equation of state with sound speed of $c_s = 10$ km s$^{-1}$.

The axisymmetric part of the external gravitational potential gives rise to a rotational velocity profile that resembles normal disk galaxies with velocity of $v_c \simeq 200$ km s$^{-1}$ at the flat part. The non-axisymmetric part consists of two components: a bar and spiral arms. As in Paper I, the bar potential is modeled by a Ferrers prolate spheroid whose parameters are fixed to the central density concentration index $n = 1$, the semi-major and minor axes 5 kpc and 2 kpc, respectively, the mass $1.5 \times 10^{10}$ $M_\odot$, and the pattern speed $\Omega_{\rm bar} = 33$ km s$^{-1}$ kpc$^{-1}$. For the spiral potential, we take a two-armed trailing logarithmic model of Shetty & Ostriker (2006):

$$\Phi_s(R,\phi;t) = \Phi_{s0}\cos\left(m\left[\phi + \frac{\ln R}{\tan p_*} - \Omega_{\rm arm}t + \phi_0\right]\right), \quad (2)$$

for $R \geq 6$ kpc and $\Phi_s = 0$ at $R < 5$ kpc, with $\Phi_s$ between 5 kpc and 6 kpc tapered by a Gaussian function. Here, $m$, $p_*$, $\Omega_{\rm arm}$, and $\phi_0$ denote the number, the pitch angle, the pattern speed, and the initial phase of the arms, respectively. The amplitude $\Phi_{s0}$ of the arm potential is controlled by the dimensionless arm-strength parameter $\mathcal{F}$ defined by

$$\mathcal{F} \equiv \frac{m\Phi_{s0}}{v_c^2 \tan p_*}, \quad (3)$$

which measures the radial force due to the spiral arms relative to the centrifugal force from the background galaxy rotation (e.g., Kim & Kim 2014). In this work, we fix $m = 2$, $p_* = 20°$, $\phi_0 = 147°$, and vary $\mathcal{F}$ and $\Omega_{\rm arm}$.

Our calculations incorporate a prescription for star formation and ensuing feedback via SNe. We determine star-forming regions based on the critical density corresponding to the Jeans condition, and allow for a star formation efficiency of 1% (e.g., Krumholz & McKee 2005; Krumholz & Tan 2007). When a cloud is determined to undergo star formation, we spawn a sink particle corresponding to a star cluster, and convert 90% of the gas mass to the particle. The mass of each particle is typically in the range of $\sim 10^5 - 10^7$ $M_\odot$. Each particle interacts gravitationally with each other while orbiting under the influence of total gravity, and injects radial momentum to the surrounding gaseous medium, mimicking multiple simultaneous SN explosions from a cluster. We consider a time delay, $\Delta\tau_{\rm SN}$, between star formation and SN feedback. Under the Kroupa (2001) initial mass function, the mass-weighted mean main-sequence lifetime of stars with $M \geq 8$ $M_\odot$ that explode as SNe is estimated to be $\Delta\tau_{\rm SN} = 10$ Myr, but we also run a case with $\Delta\tau_{\rm SN} = 5$ Myr to study its effect on the ring SFR. In our models, the amount of the radial momentum per single SN in the in-plane direction is taken to be $2.25 \times 10^5$ $M_\odot$ km s$^{-1}$. This corresponds to the snowplow phase of a shell expansion due to an injection of SN energy $10^{51}$ erg in the in-plane direction (e.g., Chevalier 1974; Cioffi et al. 1988; Thornton et al. 1998; Kim et al. 2013; Kimm & Cen 2014).

Although it is challenging to measure the pattern speeds of bars and spiral arms, observations indicate that they are either corotating or the arms are rotating more slowly than the bar (e.g., Fathi et al. 2009; Martínez-García & González-López lira 2011). To explore various situations, we run a total of 14 models with differing $\mathcal{F}$ between 0 and 20%, $\Omega_{\rm arm}$ between 10 and 33 km s$^{-1}$ kpc$^{-1}$, and $\Delta\tau_{\rm SN}$ between 5 and 10 Myr. Columns (1)–(4) of Table 1 list the name and the parameters of each model. Columns (5)–(9) give some of the simulation outcomes, which will be explained later. Model F00 is a bar-only model, while the other models possess spiral arms as well. Model F10P20d is a con-

**Table 1**
Model Parameters and Simulation Outcomes

| Model | $\mathcal{F}$ | $\Omega_{\rm arm}$ | $\Delta\tau_{\rm SN}$ | $\langle\Sigma_{\rm dl}\rangle$ | $\langle M_{\rm ring}\rangle$ | $M_*$ | $\langle$SFR$\rangle$ | $R_{\rm ring}$ |
|---|---|---|---|---|---|---|---|---|
| | (%) | (km s$^{-1}$ kpc$^{-1}$) | (Myr) | (M$_\odot$ pc$^{-2}$) | ($10^9$ M$_\odot$) | ($10^9$ M$_\odot$) | (M$_\odot$ yr$^{-1}$) | (kpc) |
| (1) | (2) | (3) | (4) | (5) | (6) | (7) | (8) | (9) |
| F00 | 0 | - | 10 | 21.8±9.34 | 0.25±0.01 | 0.92 | 0.19±0.21 | 0.67 |
| F05P10 | 5 | 10 | 10 | 41.3±34.6 | 0.21±0.06 | 1.53 | 0.98±0.76 | 0.90 |
| F05P20 | 5 | 20 | 10 | 34.8±31.2 | 0.23±0.03 | 1.27 | 0.62±0.35 | 0.89 |
| F05P33 | 5 | 33 | 10 | 23.1±13.3 | 0.27±0.01 | 1.02 | 0.31±0.20 | 0.72 |
| F10P10 | 10 | 10 | 10 | 66.7±55.5 | 0.26±0.08 | 2.07 | 1.32±1.09 | 1.00 |
| F10P20 | 10 | 20 | 10 | 75.4±79.2 | 0.27±0.05 | 1.70 | 1.32±1.07 | 0.95 |
| F10P33 | 10 | 33 | 10 | 24.0±20.5 | 0.28±0.01 | 1.01 | 0.31±0.17 | 0.73 |
| F15P10 | 15 | 10 | 10 | 101.7±133.8 | 0.24±0.07 | 2.84 | 2.44±1.93 | 0.98 |
| F15P20 | 15 | 20 | 10 | 94.2±90.1 | 0.25±0.07 | 2.31 | 2.11±1.41 | 1.02 |
| F15P33 | 15 | 33 | 10 | 24.4±19.1 | 0.26±0.01 | 1.16 | 0.34±0.40 | 0.70 |
| F20P10 | 20 | 10 | 10 | 123.9±314.1 | 0.23±0.08 | 3.55 | 3.54±1.69 | 1.08 |
| F20P20 | 20 | 20 | 10 | 114.3±220.3 | 0.27±0.07 | 3.04 | 2.95±1.84 | 0.94 |
| F20P33 | 20 | 33 | 10 | 30.1±27.7 | 0.23±0.03 | 1.42 | 0.75±0.42 | 0.81 |
| F10P20d | 10 | 20 | 5 | 68.3±80.4 | 0.25±0.06 | 1.76 | 1.45±1.21 | 0.95 |

**Note**. — $\mathcal{F}$ denotes the dimensionless arm strength; $\Omega_{\rm arm}$ is the arm pattern speed; $\Delta\tau_{\rm SN}$ is the time interval between the cluster formation and SN explosion; $\langle\Sigma_{\rm dl}\rangle$ is the mean surface density of the dust-lane segments at $R = 2.0-2.5$ kpc averaged over $t = 0.4-1.0$ Gyr; $\langle M_{\rm ring}\rangle$ is the gas mass in the ring averaged over $t = 0.4 - 1.0$ Gyr; $M_*$ is the total stellar mass formed until $t = 1.0$ Gyr; $\langle$SFR$\rangle$ is the ring SFR averaged over $t = 0.4 - 1.0$ Gyr; $R_{\rm ring}$ is the ring radius at $t = 1.0$ Gyr.

trol model with $\Delta\tau_{\rm SN} = 5$ Myr. Note that the models with $\Omega_{\rm arm} = 33$ km s$^{-1}$ kpc$^{-1}$ have the arms and bar corotating, with the co-rotation resonance (CR) radius at $R_{\rm CR,bar} = R_{\rm CR,arm} = 6$ kpc, while the models with $\Omega_{\rm arm} = 10$ and 20 km s$^{-1}$ kpc$^{-1}$ have the $R_{\rm CR,arm} = 20$ and 10 kpc, respectively.

As in Paper I, we integrate the basic ideal hydrodynamic equations using the CMHOG code in the frame corotating with the bar (Piner et al. 1995). To resolve the ring regions with high accuracy, we set up a logarithmically-spaced grid that extends from $R = 0.05$ to 30 kpc. The number of zones in our models is $1290 \times 632$ in the radial and azimuthal directions covering the half-plane with $\phi = -\pi/2$ to $\pi/2$, leading to the grid size of 5 pc at $R = 1$ kpc where a ring preferentially forms. We adopt the outflow and periodic boundary conditions at the radial and azimuthal boundaries, respectively. In order to avoid strong transients in the gas flow caused by a sudden introduction of the bar, the bar is slowly introduced over one bar revolution time of 0.19 Gyr.

## 3. SIMULATION RESULTS

We in this section first describe the overall evolution of our fiducial model F10P20 with $\mathcal{F} = 10\%$ and $\Omega_{\rm arm} = 20$ km s$^{-1}$ kpc$^{-1}$ in comparison with its no-arm counterpart, Model F00. Evolution of other models with arms is quantitatively similar to that of Model F10P20. We then present the results on star formation histories and distributions of star clusters that form in nuclear rings.

### 3.1. *Overall Evolution*

Figure 1 shows snapshots of the gaseous surface density in logarithmic scale at $t = 0.15$, 0.4, and 0.7 Gyr of Models F00 with no arms (left) and Model F10P20 with arms (middle). The right panels zoom in the central 2 kpc regions of Model F10P20 to display the positions of star-forming regions younger than 20 Myr (colored asterisks) as well as all star clusters that have formed (small dots). The bar is pointing toward the $y$-axis and remains stationary in the simulation domain. The solid oval in the lower-left panel draws the outermost $x_1$ orbit under the given potential, which cuts the $x$- and $y$-axes at 3.6 kpc and 4.7 kpc, respectively. The total gas mass enclosed by the outermost $x_1$ orbit is $1.2 \times 10^9$ M$_\odot$ in the initial disk. Note that the inner ends of the gaseous spiral arms are connected to the bar ends for most of the time, even though the arms and the bar have different pattern speeds.

An introduction of the bar and spiral potentials provides strong perturbations for gas orbits that would otherwise remain circular. The gas in the bar region is readily shocked to form "dust lanes" referring to high-density ridges, indicated as arrows in the upper panels of Figure 1, located at the leading side of the bar major axis (e.g., Athanassoula 1992). Gas passes through the dust-lane shocks almost perpendicularly and loses angular momentum, moving radially inward to form a nuclear ring at the location where centrifugal force balances the gravity (Kim et al. 2012a,b). At the same time, the gas in the arm region develops spiral shocks whose pitch angle is smaller than that of the stellar arms. The offset between

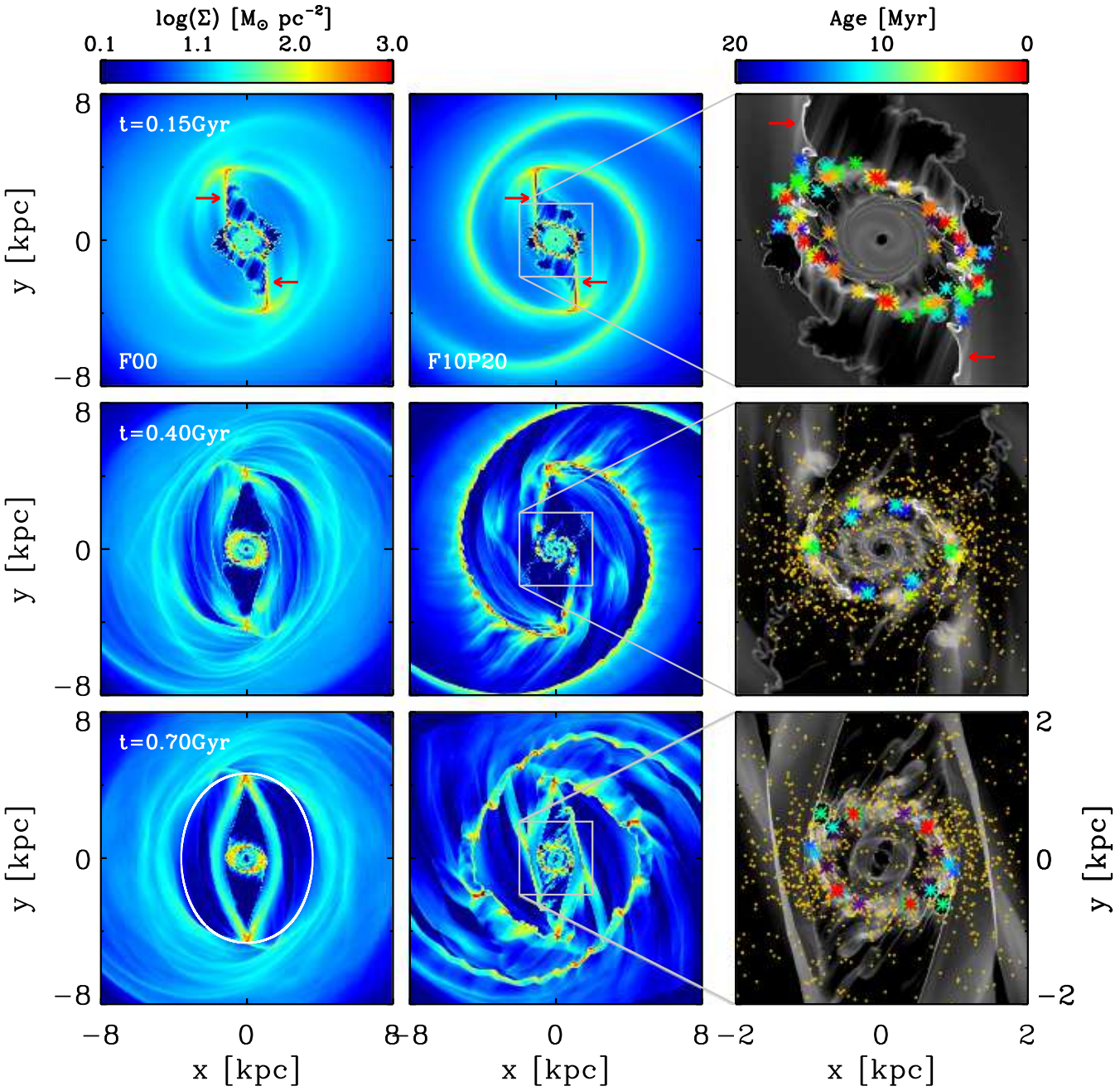


**Figure 1.** Snapshots of gas surface density at $t = 0.15$ Gyr (top), 0.40 Gyr (middle), and 0.70 Gyr (bottom) for Model F00 (left column) and Model F10P20 (middle column). The right panels expand the central 2 kpc regions of Model F10P20 to show the distributions of young clusters with age less than 20 Myr (asterisks) and older clusters (dots) that formed. The CR of the bar is at $R_{\rm CR,bar} = 6$ kpc inside which the gas is rotating in the counterclockwise direction. A pair of the red arrows in each of top panels indicate high-density ridges, termed dust lanes, located at the downstream side from the bar major axis. The oval in the lower-left panel draws the outermost $x_1$ orbit, outside of which the gas distribution is not much perturbed in Model F00. The left and right colorbars label $\log\Sigma$ and the age of young clusters, respectively.

the pitch angles of gaseous and stellar arms is larger for smaller $\mathcal{F}$ and larger $\Omega_{\rm arm}$ (Kim & Kim 2014). In general, spiral shocks in the arm region are much weaker than the dust-lane shocks in the bar region owing largely to a smaller angle between the gas streamlines and the shock fronts in the former, so that gas infall due to the spiral shocks occurs much more slowly than that associated with the bar. At about 0.11 Gyr, stars start to form in the ring where plenty of gas is accumulated by the bar potential to meet the Jeans condition for gravitational collapse.

At early time ($t = 0.15$ Gyr), the effect of spiral arms on the bar region is almost negligible since they are still weak and growing. When the arms become strong enough to induce spiral shocks, the gas originally located outside the bar region but inside the CR of the arms (i.e., $R_{\rm CR,bar} < R < R_{\rm CR,arm}$) starts to move radially inward by losing angular momentum due to the spiral poten-

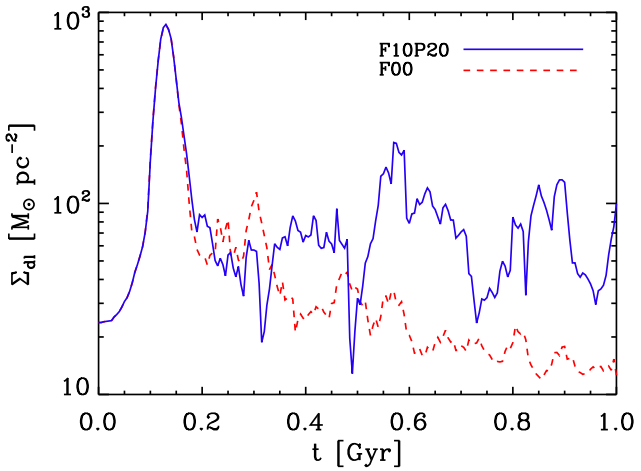


**Figure 2.** Temporal changes of the gas surface density of the dust lanes $\Sigma_{\rm dl}$ averaged over $R = 2.0-2.5$ kpc for Models F10P20 and F00. In Model F00, the dust lanes are strong only when the gas in the bar region infalls ($t \sim 0.1-0.2$ Gyr) and when the ring gas is expelled to the bar region by star formation feedback ($t \sim 0.2-0.3$ Gyr). The arm-induced mass inflows make the dust lane strong at late time in Model F10P20.

tial and associated spiral shocks, while the gas outside $R_{\rm CR,arm}$ drifts outward. The inflowing gas due to the arms moves on along $x_1$ orbits after entering the bar region. The gas is piled up at the bar ends where $x_1$ orbits crowd. Mutual collisions of gas orbits there further take away angular momentum from the gas, intermittently sending gas blobs along the dust lanes to the nuclear ring. When this happens, the dust lanes become inhomogeneous, as illustrated in the $t = 0.4$ Gyr snapshot of Model F10P20 in Figure 1. This not only enhances the gas surface density of the dust lanes but also fuels episodic star formation in the ring at late time (see below).

Dust lanes are located at the downstream side of galaxy rotation from the bar major axis, and are more straight in more strongly barred galaxies (Knapen et al. 2002; Comerón et al. 2009; Kim et al. 2012a). In our models, they typically have a width of $\sim$ 50 pc and extend from the bar ends to the nuclear ring located at $R \sim 1$ kpc. Figure 2 plots temporal variations of the mean gas surface density, $\Sigma_{\rm dl}$, of the dust-lane segments at $R = 2.0-2.5$ kpc in Models F00 (dashed) and F10P20 (solid). In Model F00, $\Sigma_{\rm dl}$ is large only when the gas in the bar region experiences the massive infall to the nuclear ring ($t \sim 0.1-0.2$ Gyr) and when the feedback from the initial starburst activities sends the ring material out to the dust lanes ($t \sim 0.2-0.3$ Gyr), after which $\Sigma_{\rm dl}$ decays to very small values. The early behavior of $\Sigma_{\rm dl}$ in Model F10P20 is similar to that in Model F00, but the gas inflows induced by spiral arms make the dust lanes in the former much more pronounced at $t \gtrsim 0.4$ Gyr than in the no-arm counterpart. This trend can also be seen in Figure 1 where the dust lanes in Model F00 are strong at $t = 0.15$ Gyr but can be barely identified at $t \gtrsim 0.4$ Gyr, while they are vividly apparent at any time in Model F10P20. Column (5) of Table 1 gives the mean surface density $\langle\Sigma_{\rm dl}\rangle$ as well as standard deviations of the dust lanes for all models, where the angle brackets $\langle\,\rangle$ represent a time average over $t = 0.4-1.0$ Gyr.

In the $t = 0.7$ Gyr snapshot of Model F00, there is a well-defined, elongated gaseous feature, called a gaseous inner ring, that lies inside the outermost $x_1$ orbit and encompasses the dust lanes (e.g., Buta 1986, 2013; Regen et al. 2002). The inner ring has roughly the same size as the bar (e.g., Buta & Combes 1996). As explained in Paper I, it begins to form after dust lanes find their equilibrium positions by collecting the residual gas that did not experience the dust-lane shocks. In Model F10P20, however, the inner ring is strongly perturbed by the arm-induced mass inflows at late time. It is also influenced by feedback from star formation in the nuclear ring. As Figure 1 shows, the spiral shocks at $t = 0.4$ Gyr are abundant with dense clumps produced by a wiggle instability of the shock fronts, which occurs as a consequence of the potential vorticity accumulation in the gas flows moving across curved shock fronts multiple times (Kim et al. 2014a). These clumps collide and merge with each other as they move along the arms, and become loose at the interface between the arm and bar regions. When they enter the bar region, they thus have significant inward radial velocities, providing strong perturbations to the gas already in the inner ring. They eventually settle on $x_1$ orbits, lose angular momentum by hitting the bar ends, and move further in to the nuclear ring.

### 3.2. *Star Formation*

#### 3.2.1. *Enhanced SFR by Arms*

Figure 3 plots the temporal evolution of the SFR in the ring, the total stellar mass $M_*(t)$ formed until time $t$, and the total gas mass $M_{\rm ring}$ in the ring for models with $\mathcal{F} = 10\%$ but differing $\Omega_{\rm arm}$.[1] The results of Model F00 with $\mathcal{F} = 0$ are compared as dashed lines. The overall behavior of the SFR in the bar-only model is characterized by a strong primary burst and a few subsequent secondary bursts before declining to small values at $t \gtrsim 0.3$ Gyr, with the duration of the burst phase corresponding to the bar growth time (Paper I). The presence of spiral arms especially when the pattern speed is small can make the SFR rejuvenated at $t \gtrsim 0.4$ Gyr. As we mentioned above, the mass infalls from the bar ends to the ring occur intermittently, resulting in episodic star formation in the ring at late time. Since the typical inflow velocity due to the arms is $\sim 1$ km s$^{-1}$ (Kim & Kim 2014), the arm-induced SFR in the ring can persist longer than the Hubble time, as long as $R_{\rm CR,arm}$ is located sufficiently far away from the bar ends. Note that ring SFR is not enhanced much in Model F10P33, since $R_{\rm CR,arm}$ is located just outside the bar ends.

Figure 3(c) shows that in all models $M_{\rm ring}$ is maintained relatively constant at $\sim (2-4)\times10^8$ M$_\odot$ throughout evolution, similar to observations (e.g., Sheth et al. 2005). Column (6) of Table 1 gives $\langle M_{\rm ring}\rangle$ for all models. Since the SFR depends on $\Omega_{\rm arm}$ considerably, this suggests that it is not the gas mass in the ring but the mass inflow rate to the ring that controls the ring SFR, even when the effect of spiral arms is included.

[1] We calculate the ring mass as $M_{\rm ring} \equiv \int_{0.5\ {\rm kpc}}^{1.5\ {\rm kpc}} \int \Sigma R d\phi dR$, since the ring density in our models is about two orders of magnitude larger than the density of the surrounding medium near the galaxy center.

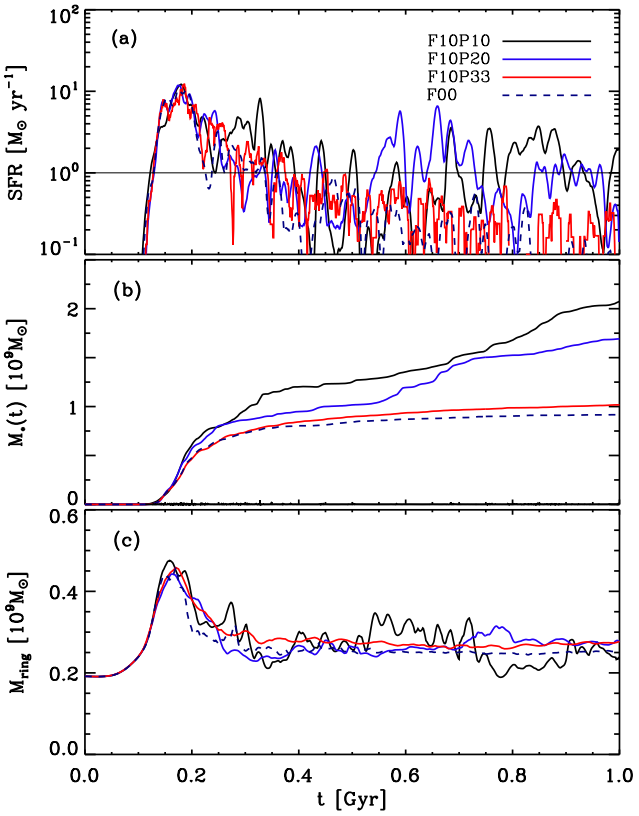


**Figure 3.** Temporal variations of the (a) SFR in the ring, (b) total stellar mass $M_*(t)$ formed until $t$, and (c) total gas mass $M_{\rm ring}$ in the ring for models with $\mathcal{F} = 10\%$ and varying $\Omega_{\rm arm}$. The results of the bar-only model are compared as dashed lines. Arm-induced gas inflows make the SFR rejuvenated at $t \gtrsim 0.4$ Gyr. The ring SFR is not well correlated with $M_{\rm ring}$.

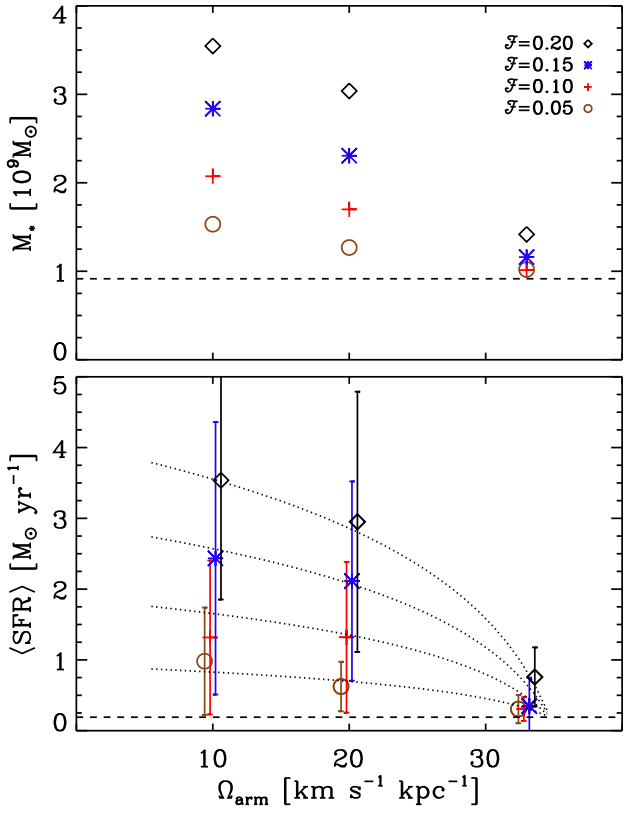


**Figure 4.** (a) Total stellar mass $M_*$ formed until $t = 1$ Gyr and (b) the mean values (symbols) and standard deviations (errorbars) of the SFR averaged over $t = 0.4 - 1$ Gyr as functions of the arm strength $\mathcal{F}$ and pattern speed $\Omega_{\rm arm}$. The horizontal dashed line in each panel marks the value in the bar-only model. In (b), the data are displaced slightly in the horizontal direction for clarity. The dotted lines are our best fits (Eq. (4)).

With the typical ring radius of 1 kpc and thickness of 50 pc, this translates into the averaged gas surface density $\Sigma_{\rm ring} \sim 650-1250$ M$_\odot$ pc$^{-2}$, which is approximately equal to the critical density $\Sigma_c = 10^3$ M$_\odot$ pc$^{-2}$ for Jeans collapse. When $\Sigma_{\rm ring} > \Sigma_c$, star formation takes place in the ring, reducing the gas density. When $\Sigma_{\rm ring} < \Sigma_c$, star formation is halted in the ring which has to wait until fresh gas is filled in to resume star formation. For the bar-only models, Paper I found that the ring shrinks in size steadily over time due to the addition of gas with low angular momentum. Enhanced SFR by arms turns out to reduce the shrinking rate of the ring size (see Section 3.2.2).

Figure 4 plots $M_*$ at $t = 1$ Gyr and the mean values $\langle$SFR$\rangle$ (symbols) along with the standard deviations (errorbars) of the SFR averaged over $t = 0.4 - 1.0$ Gyr for all models. These values are also tabulated in Columns (7) and (8) of Table 1. The horizontal dashed line in each panel represents the case with no arm. Note that $M_* = 0.9 \times 10^9$ M$_\odot$ in Model F00, which is about 75% of the initial gas mass inside the outermost $x_1$ orbit. While $M_*/(1$ Gyr$)$ corresponds to the mean SFR throughout entire evolution, $\langle$SFR$\rangle$ measures the mean value of the arm-induced SFR after the initial gas infall due to the bar potential is almost finished. Clearly, both $M_*$ and $\langle$SFR$\rangle$ are larger for models with larger $\mathcal{F}$ and/or smaller $\Omega_{\rm arm}$. For $\Omega_{\rm arm} = 10$ and 20 km s$^{-1}$ kpc$^{-1}$, for example, the time-averaged ring SFR over $t = 0.4 - 1.0$ Gyr is enhanced by a factor of 5.2, 6.9, 12.8, 18.6, and 3.3, 6.9, 11.1, 15.5 for models with $\mathcal{F} = 5, 10, 15, 20\%$, respectively, compared to the no-arm counterpart. The dotted lines are our best fits to $\langle$SFR$\rangle$:

$$\frac{\langle \rm SFR \rangle}{\rm M_\odot\ yr^{-1}} = 0.19 + 25\mathcal{F}^{1.2} \log\left(11.5 - 10\frac{\Omega_{\rm arm}}{\Omega_{\rm bar}}\right). \quad (4)$$

The increasing trend of the ring SFR with $\mathcal{F}$ is similar to that of the gas inflow rates driven by the arms reported by Kim & Kim (2014). This makes sense since a smaller pattern speed implies a larger $R_{\rm CR,arm}$ and since stronger spiral shocks can remove a larger amount of angular momentum from the gas. When the arms are corotating with the bar, on the other hand, the presence of spiral arms does not affect the ring SFR much. This shows that the enhancement of the ring SFR due to spiral arms is significant only when they have different pattern speeds.

### 3.2.2. *Age Gradients*

Paper I showed that young star clusters exhibit a noticeable age gradient in the azimuthal direction along a nuclear ring only when the SFR is larger than the critical value $\dot{M}_{*,\rm CP}$, which is set by the maximum SFR affordable at the contact points. In the high-SFR phase (SFR $> \dot{M}_{*,\rm CP}$), star-forming regions are distributed

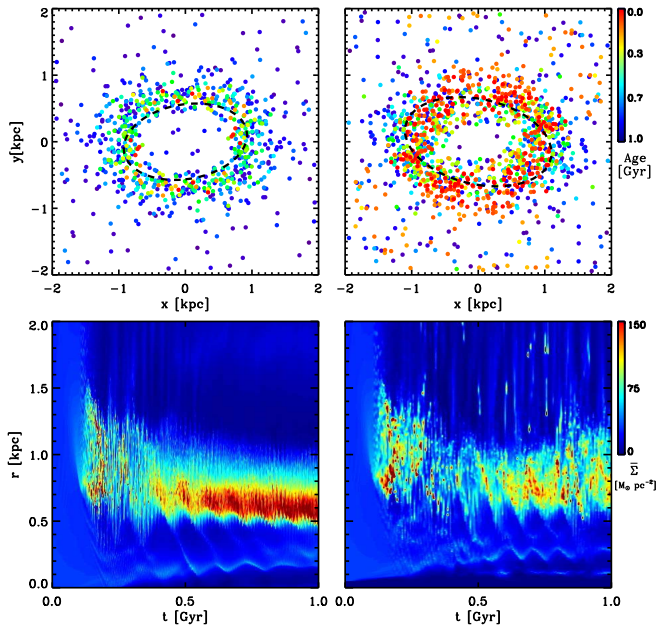


**Figure 5.** (Upper) Spatial distributions of star clusters at $t = 1$ Gyr, with color denoting their age and (lower) the radial and temporal variations of the azimuthally-averaged surface density $\bar{\Sigma}$. The left and right panels are for Model F00 and F20P20, respectively. In the upper panels, the dashed oval fits the ring at $t = 1$ Gyr in each model.

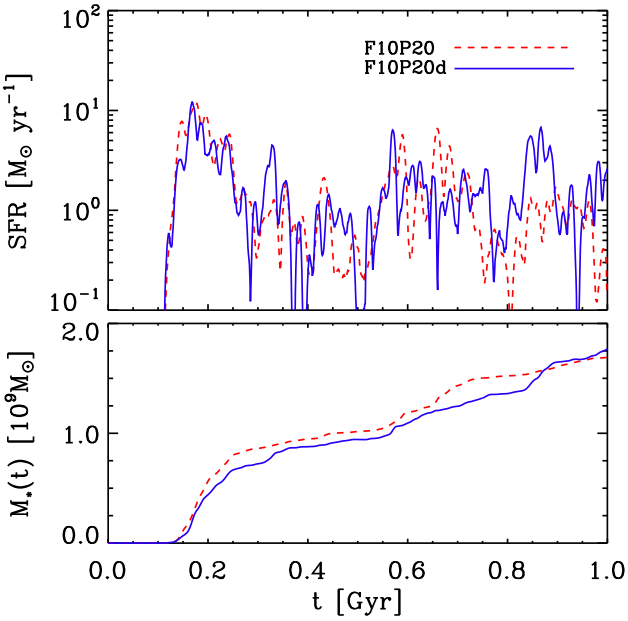


**Figure 6.** Comparison of the ring SFR and the total stellar mass $M_*(t)$ between Model F10P20 with $\Delta\tau_{\rm SN} = 10$ Myr and Model F10P20d with $\Delta\tau_{\rm SN} = 5$ Myr. While the detailed histories of the SFR are different, the time-averaged SFR and $M_*$ are within 10%.

randomly throughout the ring, hence no age gradient of clusters is expected. In the low-SFR phase (SFR $< \dot{M}_{*,\rm CP}$), on the other hand, they are localized to the contact points, leading to a well-defined azimuthal age gradient. These two modes of star formation are referred to respectively as "popcorn" and "pearls-on-a-string" models by Böker et al. (2008). For our adopted parameters, Paper I found $\dot{M}_{*,\rm CP} \sim 1$ M$_\odot$ yr$^{-1}$, although it depends sensitively on the ring size and the gas sound speed. Paper I also showed that star clusters with age $< 1$ Gyr show a positive radial age gradient such that older clusters are located at larger $R$ owing to a secular decrease of the ring size.

We find that the condition for the presence or absence of the azimuthal age gradient of young clusters is not affected by arm-enhanced star formation. By analyzing the dependence of the cluster ages younger than 10 Myr on the azimuthal positions in all models with spirals, we find that star formation occurs in the pearls-on-a-string fashion for $\sim 80\%$ of the low-SFR phase and for $\sim 20\%$ of the high-SFR phase. In the high-SFR phase, the mass inflow rate along the dust lanes is too large for star formation to consume all the inflowing gas at the contact points: overflowing gas produces star-forming clumps distributed randomly along the nuclear ring. In the low SFR phase, however, most of the inflowing gas undergoes star formation at the contact points. Since clusters age as they move along the ring, this naturally leads to an azimuthal age gradient.

However, the arm-enhanced star formation tends to remove the radial age gradient of star clusters. The upper panels of Figure 5 display the spatial distributions of star clusters at $t = 1$ Gyr in Model F00 (left) and Model F20P20 (right), with the color representing their age. The lower panels plot the corresponding temporal changes of the azimuthally-averaged gas surface density $\bar{\Sigma}(R) \equiv \int \Sigma d\phi/(2\pi)$ in linear scale. In the no-arm model, younger clusters are located preferentially at smaller $R$ due to a secular decrease in the ring size. This results in a radial age gradient amounting to $d\log(t/{\rm yr})/d(R/{\rm kpc}) \sim 15$ in Model F00. In Model F20P20, on the other hand, gas driven in by the spiral arms has larger angular momentum than in the ring gas, so that the ring does not decrease in size after $\sim 0.4$ Gyr. In addition, active star formation feedback disperses the ring gas widely in the radial direction, making the ring larger than in the no-arm model. Column (9) of Table 1 gives the average ring radius $R_{\rm ring}$ at $t = 1$ Gyr, where $R_{\rm ring} \equiv \int R\bar{\Sigma}dR/\int \bar{\Sigma}dR$, with the radial integration taken over $R = 0.5 - 1.5$ kpc, showing that the radii of the rings in spiral-arm models with $\Omega_{\rm arm} \lesssim 20$ km s$^{-1}$ kpc$^{-1}$ are larger by about 45% than in Model F00. Consequently, star clusters in models with arm-enhanced star formation exhibit no apparent radial age gradient, as the upper-right panel of Figure 5 illustrates.

### 3.2.3. *Effects of* $\Delta\tau_{\rm SN}$

To explore the effects of the time delay between star formation and SN explosion, we run Model F10P20d with $\Delta\tau_{\rm SN} = 5$ Myr, while the other parameters are taken identical to those in Model F10P20. Figure 6 compares the temporal changes of the SFR and $M_*(t)$ from these two models. Due to a shorter delay, feedback occurs earlier in Model F10P20d, which tends to reduce SFR and $M_*$ at early time compared to those in Model F10P20. Although detailed star formation histories are different, the time averaged SFRs over $t = 0.4 - 1.0$ Gyr are 1.32 and 1.45 M$_\odot$ yr$^{-1}$ for Models F10P20 and F10P20d, respectively, which agree within 10%. The total stellar

mass formed at the end of the runs are also similar at $M_* = 1.70 \times 10^9$ M$_\odot$ and $1.76 \times 10^9$ M$_\odot$ for Models F10P20 and F10P20d, respectively. This demonstrates that the results on the arm-enhanced SFR presented in this work is insensitive to the choice of $\Delta\tau_{\rm SN}$ as long as it is within a reasonable range.

## 4. SUMMARY AND DISCUSSION

We have presented the results of two-dimensional grid-based hydrodynamic simulations to study star formation in nuclear rings of barred-spiral galaxies. The gaseous medium is taken to be isothermal, self-gravitating, unmagnetized, and limited to an infinitesimally-thin disk. We incorporate a prescription for star formation and delayed feedback via SNe in the form of momentum injection. We handle the bar and spiral patterns using rigidly-rotating, fixed gravitational potentials, and do not consider the back reaction of the gas to the underlying patterns. To study various situations, we vary only the strength and pattern speed of the arms, while fixing other arm and bar parameters. The main results and corresponding discussions are as follows.

1. – *Arm-enhanced SFR*: Spiral arms located in the outer disks can drive gas toward the bar region, enhancing star formation in nuclear rings considerably, only if the arm pattern speed is smaller than that of the bar. This is because only the gas located between the bar ends and the CR of the arms can lose angular momentum by passing through spiral arms and move inward to the bar region, while the gas outside the CR of the arms move radially outward. The gas entering the bar region is first gathered to the bar ends where it loses its angular momentum additionally to move further in along the dust-lane shocks to the nuclear ring. The inflow to the ring occurs in an intermittent fashion, making the ring star formation episodic that lasts long until the end of the simulations. Ignoring the star formation induced at early time by the bar, the enhanced SFR by spiral arms is $\sim (0.6 - 3.5)$ M$_\odot$ yr$^{-1}$, which is about 3 to 20 times larger than that in the no-arm counterpart. This has an important implication that the SFR histories in nuclear rings can be significantly affected by spiral arms that are slow and strong. Some galaxies are observed to have undergone several episodic bursts of star formation in the rings over a few Gyrs (Allard et al. 2006; Sarzi et al. 2007; van der Laan et al. 2013), which appear difficult to be explained by gas inflows driven solely by the bar potential (Paper I). We suggest that these sustained starburst activities might have resulted from additional gas feeding due to spiral arms.

2. – *Dust Lane Strength*: The mass inflows driven by arms also help make the dust lanes stronger. By analyzing Sloan Digital Sky Survey DR7 data, Comerón et al. (2009) found that about 20% of 266 galaxies with measured bar strength host dust lanes with appreciable strength. On the other hand, numerical simulations with only a bar potential show that dust lanes remain strong only for $\sim 0.2$ Gyr around the time when the bar potential achieves its full strength (e.g, Paper I; Kim & Stone 2012). Given that bars persist for several Gyrs (e.g., Gadotti & de Souza 2005; Pérez et al. 2009; Berentzen et al. 2007; Athanassoula et al. 2013), this is not compatible with the results of Comerón et al. (2009). Barred galaxies with strong dust lanes may be either dynamically young or supplied with fresh gas. Our numerical results in this paper suggest that spiral arms with large $R_{\rm CR,arm}$ can be efficient to transport the gas from outside to the bar region. The typical density of dust lanes in our standard model F10P20 is about 70 M$_\odot$ pc$^{-2}$. This corresponds to the extinction magnitude of $A_V \sim 5$ in the visual band assuming a standard value of $\sim 3$ for the ratio of total to selective extinction, readily visible against the background stellar light.

3. – *Age Gradients of Star Clusters*: The gas driven in from the arms to the ring is found to have larger angular momentum than the gas already in the ring. In addition, feedback from active star formation at late time tends to reduce the rate of angular momentum removal, making the rings in models with spiral arms larger by $\sim 45\%$ than those in bar-only models. Consequently, star clusters formed in bar-only models retain an age gradient in the radial direction, while they do not in models with slow-rotating spiral arms. On the other hand, the arm-enhanced star formation exhibits an azimuthal age gradient of star clusters such that younger clusters are located closer to the contact points when SFR is small, while clusters with different ages are well mixed when SFR is large. The critical SFR that determines the absence/presence of the azimuthal age gradient is set by the maximum gas consumption rate $\dot{M}_{*,\rm CP}$ at the contact points, which is $\sim 1$ M$_\odot$ yr$^{-1}$ in our current models, although it may depends sensitively on the gas sound speed and the ring size as $\dot{M}_{*,\rm CP} \propto c_s^3 R_{\rm ring}^2$ (Paper I; see also Kim et al. 2014b). This appears consistent with the observational data of Mazzuca et al. (2008) in that nuclear rings with an azimuthal age gradient have, on average, a smaller SFR than those without age gradient.

Many uncertainties surround the observational determinations of the SFR in nuclear rings and the arm pattern speed. The derived SFRs from different methods do not always agree. For the nuclear ring of NGC 6951, for instance, Mazzuca et al. (2008) derived the current SFR $\sim 1.4$ M$_\odot$ yr$^{-1}$ based on the old H$\alpha$–SFR relation of Kennicutt (1998), which is known to yield a larger SFR by a factor of $\sim 1.47$ than the newly calibrated relation (e.g., Hao et al. 2011; Kennicutt & Evans 2012). Also, local variations in the stellar-age mix, initial mass function, gas/dust geometry, etc. are likely to contaminate the derived SFRs to some extent (Kennicutt & Evans 2012). On the other hand, van der Laan et al. (2013) measured the ages and masses of stellar clusters directly to obtain a temporal history of SFR in the ring of the same galaxy. They found SFR $\sim 0 - 0.15$ M$_\odot$ yr$^{-1}$ during the past 1 Gyr, with the current SFR less than 0.03 M$_\odot$ yr$^{-1}$, much smaller than value reported by Mazzuca et al. (2008). Regarding the pattern speeds, a model-independent kinematic method proposed by Tremaine & Weinberg (1984) has been widely used to measure the angular velocities of arms and bars (e.g., Zimmer et al. 2004; Rand & Wallin 2004; Merrifield et al. 2006; Meidt et al. 2008; Fathi et al. 2009; Speights & Westpfahl 2011). This method relies critically on a few assumptions, notably that a galactic disk is in a steady state and that there is a well-defined pattern, the validity of which is not always guaranteed. For instance, star formation and ensuing feedback make the density and velocity fields non-

steady in a galactic disk. When arms are not corotating with a bar, there are significant non-steady motions in the gas flows in the region where the bar joins the arms, which is likely to compromise the derived pattern speeds based on gas tracers.

In addition to pattern speeds, there are many other factors such as the ring size, bar strength, magnetic fields that may affect the ring SFR. Therefore, it is not yet viable to make a definitive comparison of SFRs between our numerical predictions and observations. Nevertheless, the observational data tabulated in Table 1 of Mazzuca et al. (2008) show that the averaged ring SFR of SAB and SB galaxies are $2.90 \pm 2.00$ $M_\odot$ $yr^{-1}$ and $2.00 \pm 1.71$ $M_\odot$ $yr^{-1}$, respectively. Since the relative importance of spiral arms is larger for SAB than SB galaxies, these observations are not inconsistent with the idea of arm-enhanced SFR in the nuclear rings. In addition, the spiral arms of NGC 4314 seem to corotate with the bar (Buta & Zhang 2009), and the ring SFR in this galaxy is quite low at $\sim 0.1$ $M_\odot$ $yr^{-1}$ (Mazzuca et al. 2008). On the other hand, NGC 4321 known to undergo starburst activities in the ring (Ryder & Knapen 1999) have spiral arms rotating slower than the bar (Hernandez et al. 2005). These are consistent with our result that the arm pattern speed affects the ring SFR.

To explore star formation in nuclear rings, we have adopted a very simplified model of gas in barred-spiral galaxies. First of all, we treated the gas as being isothermal and unmagnetized, whereas the interstellar gas in real disk galaxies is multi-phase, magnetized, and turbulent (e.g., Wolfire et al. 2003; McKee & Ostriker 2007). This required us to handle star formation feedback in the form of momentum injection rather than thermal energy injection (e.g., Thacker & Couchman 2001; Agertz et al. 2011; Kimm & Cen 2014). We considered an infinitesimally-thin disk, which precludes a potential effect of fluid motions that involve the vertical direction. Most importantly, we here adopted a simple bar potential with fixed strength and pattern speed. Recent $N$-body simulations for bar formation show that not only the bar strength but also the bar size and pattern speed vary with time over a few Gyrs (e.g., Minchev et al. 2012; Manos & Machado 2014). The parameters of spiral arms also appear to change as a bar evolves (e.g., Athanassoula 2012; Roca-Fàbrega 2013). Therefore, it would be interesting to study how star formation in nuclear rings studied in this work would change in a more realistic environment where a bar, consisting of live stellar particles, is self-generated and interacts with the gaseous component under radiative cooling and heating, which would be an important direction of future research.

We gratefully acknowledge an insightful report form the referee. This work was supported by the National Research Foundation of Korea (NRF) grant, No. 2008-0060544, funded by the Korea government (MSIP). A part of this work was conducted while participating in the program entitled "Gravity's Loyal Opposition: The Physics of Star Formation Feedback" held at the KITP, Santa Barbara, USA, which was supported in part by the National Science Foundation under Grant No. NSF PHY11-25915.

REFERENCES

Agertz, O., Teyssier, R., & Moore, B. 2011, MNRAS, 410, 1391
Allard, E. L., Knapen, J. H., Peletier, R. F., & Sarzi, M. 2006, MNRAS, 371, 1087
Athanassoula, E. 1992, MNRAS, 259, 345
Athanassoula, E. 2012, MNRAS, 426, L46
Athanassoula, E., Machado, R. E. G., & Rodionov, S. A. 2013, MNRAS, 429, 1949
Benedict, G. F., Howell, D. A., Jørgensen, I., Kenney, J. D. P., & Smith, B. J. 2002, AJ, 123, 1411
Berentzen, I., Shlosman, I., Martinez-Valpuesta, I., & Heller, C. H. 2007, ApJ, 666, 189
Bigiel, F., & Blitz, L. 2012, ApJ, 756, 183
Böker, T., Falcón-Barroso, J., Schinnerer, E., Knapen, J. H., & Ryder, S. 2008, AJ, 135, 479
Bournaud, F., Combes, F., & Semelin, B. 2005, MNRAS, 364, L18
Brandl, B. R., Martín-Hernández, N. L., Schaerer, D., Rosenberg, M., & van der Werf, P. P. 2012, A&A, 543, A61
Buta, R. 1986, ApJ, 61, 609
Buta, R. 2013, Secular Evolution of Galaxies: XXIII Canary Islands Winter School of Astrophysics, eds. J. Falcon-Barroso, & J. Knapen (Cambridge: Cambridge University Press), p. 155
Buta, R., & Combes, F. 1996, Fund. Cosmic Phys., 17, 95
Buta, R., & Zhang, X. 2009, ApJS, 182, 559
Buta, R., Treuthardt, P. M., Byrd, G. G., & Crocker, D. A. 2000, AJ, 120, 1289
Chevalier, R. A. 1974, ApJ, 188, 501
Cioffi, D. F., McKee, C. F., & Bertschinger, E. 1988, ApJ, 334, 252
Combes, F., & Gerin, M. 1985, A&A, 150, 327
Comerón, S., Martínez-Valpuesta, I., Knapen, J. H., & Beckman, J. E. 2009, ApJ, 706, L256
Comerón, S., Knapen, J. H., Beckman, J. E., Laurikainen, E., Salo, H., Martínez-Valpuesta, & Buta, R. J. 2010, MNRAS, 402, 2462
Dekel, A., Sari, R., & Ceverino, D. 2009, ApJ, 703, 785
Fathi, K., Beckman, J. E., Piñol-Ferrer N., Hernandez, O., Martínez-Valpuesta, I., & Carignan, C. 2009, ApJ, 704, 1675
Fraternali, F., & Binney, J. 2006, MNRAS, 366, 449
Fraternali, F., & Binney, J. 2008, MNRAS, 386, 935
Gadotti, D. A., & de Souza, R. E. 2005, ApJ, 629, 797
Hao, C. N., Kennicutt R. C., Johnson, B. D., et al. 2011, ApJ, 741, 124
Heller, C. H., & Shlosman, I. 1994, ApJ, 424, 84
Hernandez, O., Wozniak, H., Carignan, C., et al. 2005, ApJ, 632, 253
Hopkins, P. F., Quataert, E., & Murray, N. 2011, MNRAS, 417, 950
Hsieh, P.-Y., Matsushita, S., Liu, G. Ho, P. T. P., Oi, N., & Wu, Y.-L. 2011, ApJ, 736, 129
Knapen, J. H., Beckman, J. E., Heller, C. H., Shlosman, I., & de Jong, R. S. 1995, ApJ, 454, 623
Knapen, J. H., Pérez-Ramírez, D., & Laine, S. 2002, MNRAS, 337, 808
Kennicutt, R. C. 1998, ARA&A, 36, 189
Kennicutt, R. C., & Evans, N. J. 2012, ARA&A, 50, 531
Kim, C.-G., Ostriker, E. C., & Kim, W.-T. 2013, ApJ, 776, 1
Kim, W.-T., & Stone, J. M. 2012, ApJ, 751, 124
Kim, W.-T., Kim, Y., & Kim, J.-G. 2014a, ApJ, 789, 68
Kim, W.-T., Seo, W.-Y., & Kim, Y. 2012a, ApJ, 758, 14
Kim, W.-T., Seo, W.-Y., & Kim, Y. 2014b, Proceedings of the International Astronomical Union, 303, 43
Kim, W.-T., Seo, W.-Y., Stone, J. M., Yoon, D., & Teuben, P. J. 2012b, ApJ, 747, 60
Kim, Y., & Kim, W.-T. 2014, MNRAS, 440, 208
Kimm, T., & Cen, R. 2014, ApJ, 788, 121
Knapen, J. H., Mazzuca, L. M., Böker, T., Shlosman, I., Colina, L., Combes, F., & Axon, D. J. 2006, A&A, 448, 489
Kroupa, P. 2001, MNRAS, 322, 231
Krumholz, M. R., & McKee, C. F. 2005, ApJ, 630, 250
Krumholz, M. R., & Tan, J. C. 2007, ApJ, 654, 304
Lubow, S. H., Balbus, S. A., & Cowie, L. L. 1986, ApJ, 309, 496
Manos, T., & Machado, R. E. G. 2014, MNRAS, 438, 2201
Martínez-García, E. E., & González-Lópezlira R. A. 2011, ApJ, 734, 122

Mazzuca, L. M., Knapen, J. H., Veilleux, S., & Regan, M. W. 2008, ApJ, 174, 337
Mazzuca, L. M., Swaters, R. A., Knapen, J. H., & Veilleux, S. 2011, ApJ, 739, 104
McKee, C. F., & Ostriker, E. C. 2007, ARA&A, 45, 567
Meidt, S. E., Rand, R. J., Merrifield, M. R., Shetty, R., & Vogel, S. N. 2008, ApJ, 688, 224
Merrifield, M. R., Rand, R. J., & Meidt, S. E. 2006, MNRAS, 366, L17
Minchev, I., Famaey, B., Quillen, A. C., et al. 2012, A&A, 548, 126
Pérez, I., Sánchez-Blázquez, P., & Zurita, A. 2009, A&A, 495, 775
Phillips, A. C. 1996, in ASP Conf. Ser. 91, Barred Galaxies, ed. R. Buta, D. A. Crocker, & B. G. Elmegreen (San Francisco: ASP), 44
Piner, B. G., Stone, J. M., & Teuben, P. J. 1995, ApJ, 449, 508
Piñol-Ferrer, N., Fathi, K., Carignan, C., et al. 2014, MNRAS, 438, 971
Rand, R. J., & Wallin, J. F. 2004, ApJ, 614, 142
Regan, M. W., Sheth, K., Teuben, P. J., & Vogel, S. N. 2002, ApJ, 574, 126
Richter, P. 2012, ApJ, 750, 165
Roberts, W. W., & Shu, F. H. 1972, ApJ, 12, 49
Roca-Fàbrega, S., Valenzuela, O., Figueras, F., et al. 2013, MNRAS, 432, 2878
Ryder, S. D., & Knapen, J. H. 1999, MNRAS, 302, L7
Ryder, S. D., Illingworth, S. M., Sharp, R. G., & Farage, C. L. 2010, PASA, 27, 56
Sandstrom, K., Krause, O., Linz, H., Schinnerer, E. et al. 2010, A&A, 518, L59
Sarzi, M., Allard, E. L, Knapen, J. H., & Mazzuca, L. M. 2007, MNRAS, 380, 949
Schinnerer, E., Böker, T., Emsellem, E., & Lisenfeld, U. 2006, ApJ, 649, 181
Seo, W.-Y. & Kim, W.-T. 2013, ApJ, 769, 100 (Paper I)
Shen, J., & Sellwood, J. A. 2004, ApJ, 604, 614
Sheth, K., Vogel, S. N., Regan, M. W. et al. 2005, ApJ, 632, 217
Shetty, R. & Ostriker, E. C. 2006, ApJ, 647, 997
Shlosman, I., Begelman, M. C., & Frank, J. 1990, Nature, 345, 679
Speights, J. C., & Westpfahl, D. J. 2011, ApJ, 736, 70
Thacker, R. J., & Couchman, H. M. P. 2001, ApJ, 555, L17
Thornton, K., Gaudlitz, M., Janka, H.-T., & Steinmetz, M. 1998, ApJ, 500, 95
Tremaine, S., & Weinberg, M. D. 1984, ApJ, 282, L5
van der Laan, T. P. R., Schinnerer, E., Boone, F., et al. 2011, A&A, 529, A45
van der Laan, T. P. R., Schinnerer, E., Emsellem, E., et al. 2013, A&A, 551, A81
Wolfire, M G., McKee, C. F., Hollenbach, D., & Tielens, A. G. G. M. 2003, ApJ, 587, 278
Zimmer, P., Rand, R. J., & McGraw, J. T. 2004, ApJ, 607, 285